High fidelity equation of state for xenon

J.H. Carpenter[a], D.G. Flicker[b], S. Root[c], R.J. Magyar[d], D.L. Hanson[e], and T.R. Mattsson[f]

Sandia National Laboratories, Albuquerque, New Mexico 87185, USA

Abstract. The noble gas xenon is a particularly interesting element. At standard pressure xenon is an fcc solid which melts at 161 K and then boils at 165 K, thus displaying a rather narrow liquid range on the phase diagram. On the other hand, under pressure the melting point is significantly higher: 3000 K at 30 GPa [1]. Under shock compression, electronic excitations become important at 40 GPa [2]. Finally, xenon forms stable molecules with fluorine (XeF_2) suggesting that the electronic structure is significantly more complex than expected for a noble gas. With these reasons in mind, we studied the xenon Hugoniot using DFT/QMD [3] and validated the simulations with multi-Mbar shock compression experiments. The results show that existing equation of state models lack fidelity and so we developed a wide-range free-energy based equation of state using experimental data and results from first-principles simulations.

1 Introduction

Increasingly accurate shock experiments at multi-Mbar pressure combined with first-principles simulations have resulted in improved knowledge of how matter behaves under extreme conditions. Over the last few years, the light elements hydrogen/deuterium [4,5] and carbon [6] as well as simple compounds like water [7] and polyethylene [8] were investigated. The agreement between first-principles simulations and experiments is remarkable, prompting an interest in investigating heavier elements with similar high-fidelity methods.

While the properties of xenon under (cold) compression have long been the focus of theoretical and experimental studies, the behavior under shock conditions is not experimentally known beyond 130 GPa [2], where existing equation of state models differ significantly. In this paper, we will briefly describe very recent experiments [9] and first-principles simulations [3,9], aimed at increasing the understanding of xenon under high pressure. We will also describe in detail the construction of a wide-range tabular equation of state for xenon.

2 Principal Hugoniot for liquid xenon

The principal Hugoniot, or shock adiabat, is the locus of end points of thermodynamic states resulting from shocks of different strengths. The location of the Hugoniot is determined by conservation laws of mass, momentum, and the first law of thermodynamics. It is a well-defined thermodynamic state and therefore a most important property to take into account when constructing an equation of state.

---

[a] e-mail: jhcarpe@sandia.gov

[b] e-mail: dgflick@sandia.gov

[c] e-mail: sroot@sandia.gov

[d] e-mail: rjmagya@sandia.gov

[e] e-mail: dlhanso@sandia.gov

[f] e-mail: trmatts@sandia.gov

2.1 Shock experiments on the Z-accelerator

The Z-accelerator at Sandia has been used to study properties of shocked materials for over a decade and the approach has been successively refined [10]. Current pulses are carefully tailored to produce shock-less acceleration of flyer plates to very high impact velocities. Flyer plate and shock velocities are measured using a velocity interferometer system for any reflector [11] (VISAR). The ability to directly measure flyer plate velocities and shock velocities in samples, along with the ability to record VISAR data using multiple velocity/fringe settings results in measurements with small systematic and statistical errors.

The cryogenic xenon targets consisted of a copper cell with a $\sim 450\,\mu$m Z-cut quartz front drive plate and 1.5 mm Z-cut quartz top-hat rear window. (In one experiment, the quartz front window was replaced with an aluminum 6061-T6 buffer plate). A reference spacer between the two quartz windows provided a sample thickness of $\sim 200\,\mu$m. The sample space was filled with high purity (>99.999%) xenon gas, obtained from Matheson Tri-Gas, to a pressure of $\sim$ 16.5 psi and cooled to 163.5 K using a liquid nitrogen cryo-system [12]. The isotope composition, as measured by mass spectrometry, gives an average atomic weight within better than 0.013 percent of the natural abundance value [13]. The xenon initial density was calculated using a linear fit of density – temperature data [14] and ranged from 2.965 g/cc to 2.972 g/cc with an uncertainty of 0.1%. Aluminum 6061-T6 flyer plates with initial thickness of $850\,\mu$m or $1000\,\mu$m were accelerated to velocities up to 30 km/s creating a planar impact with the front window.

The pressure-density (P–ρ) state of the shock compressed xenon was determined using a monte carlo impedance matching method solving the Rankine-Hugoniot equations [15]. In this method, the measured shock velocity in the quartz and a cubic fit to the quartz data in Ref. [16] were used to calculate a quartz particle velocity U_P. The quartz cubic fit was reflected about the particle velocity and the intersection of the reflected quartz Hugoniot and the line generated from the xenon shock velocity ($P = \rho_0^{Xe} U_S^{Xe} U_P$) determined P and U_P in the xenon. The density was calculated from the relation $\rho = (\rho_0 U_S)/(U_S - U_P)$.

The uncertainty in the U_P, ρ, and P was determined from the *monte carlo* aspect of the calculation. For each calculation, the measured quartz and xenon shock velocities and the initial xenon density were varied by a random number with a mean of zero and standard deviation equal to the measurement uncertainty. Error in the quartz Hugoniot fit was accounted for by varying the fit parameters about their mean using correlated random numbers with means of zero and standard deviations equal to the fit parameter uncertainty. Additional information about the experiments is given in Ref. [9].

2.2 Density functional theory simulations

The DFT-MD simulations were made with VASP 5.1.40 [17] using projector augmented wave (PAW) core potentials [18] and stringent convergence settings [3, 19]. We employed a recently developed potential (PAW Xe_GW 09 Jan 2009) at a plane wave cutoff of 400 eV and complex k-point sampling at the mean-value point ($\frac{1}{4},\frac{1}{4},\frac{1}{4}$). Electronic states were occupied according to Mermin's finite-temperature formulation of DFT [20]. We used two complementary exchange-correlation functionals: the local density approximation (LDA) and the Armiento-Mattsson (AM05) [21] functional. AM05 includes the generalized gradient in addition to the density and is designed to capture the effects of inhomogeneity by matching results for an Airy gas. AM05 has demonstrated high fidelity for wide classes of solids [22, 23] under normal conditions and was recently successfully applied to study quartz to 1.7 TPa under shock compression [16].

The principal Hugoniot is calculated with respect to a given reference state. The calculations use liquid xenon at a density of 2.97 g/cm^3 at T=163 K, similar to the experimental initial conditions. The hydrostatic Hugoniot condition is expressed as $2(E - E_{ref}) = (P + P_{ref})(v_{ref} - v)$ with E the internal energy per atom, P the system pressure, and v the volume per atom where the subscript ref denotes the initial state.
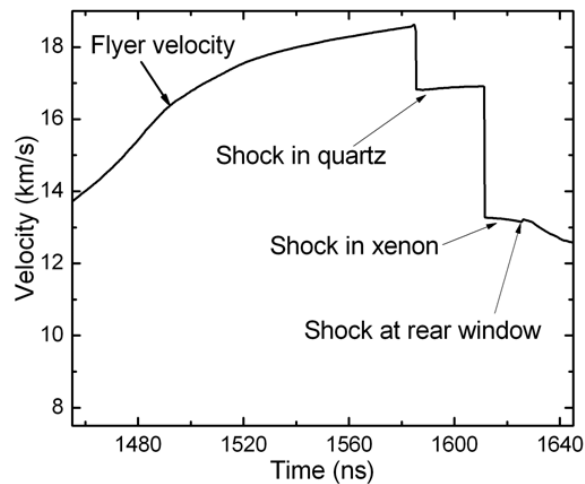
Fig. 1. Recorded velocity from VISAR. The flyer velocity is recorded as it advances towards the target. Shock fronts in quartz are reflective, hence the steady signal from the shock propagating through the front window. The shock in xenon is also reflective, giving a high-precision direct measurement of the xenon shock velocity. Finally, the shock hits the rear window.
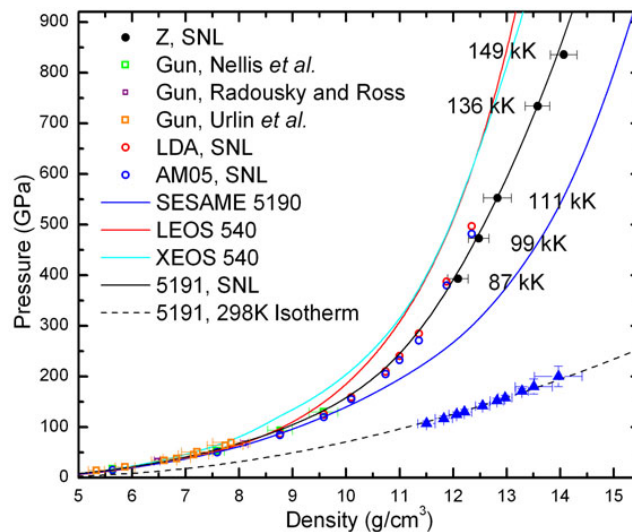

Fig. 2. Xenon Hugoniot in $P - \rho$: Filled black circles, Z data from this work; green square [2]; purple square [24]; orange square [25]; red circle, LDA (this work); blue circle, AM05 (this work); blue line, SESAME 5190; red line, LEOS 540; black line, 5191 (this work). Temperatures along the Hugoniot were calculated using 5191. Black dashed line, 5191 298 K isotherm; blue triangles, solid xenon compression data [26]. Our DFT calculated isotherm agrees well with 5191 and the experimental data [26].

2.3 Experimental results

The main result of the experimental work, the principal shock Hugoniot of xenon to 840 GPa, is presented in Fig. 2. We find that the DFT simulations are in excellent agreement with experimental gas-gun data to 130 GPa as well as the new high-pressure results. The findings are further discussed in Refs. [9] and [3]. In the next section, we will describe how the new results and the existing thermophysical data are used to construct a wide-range equation of state.

3 Model equation of state

The primary goal of developing a new multi-phase equation of state for xenon was to improve the description of the Hugoniot over current models. The EOS is based upon the standard separation of the Helmholtz free energy into ionic and electronic components

$$F = F_c + F_i + F_e, \tag{1}$$

where F_c, F_i, and F_e are respectively the cold curve, thermal ionic, and thermal electronic contributions.

First, it is worth considering what factors contribute to the unsatisfactory behavior of the current models. Three prior EOS models, LEOS 540 (540L), XEOS 540 (540X), and SESAME 5190 (5190), use the above free energy separation but their components result in Hugoniot curves that disagree with the experimental curve as well as amongst themselves. The 540L table used a model based upon QEOS, which couples Cowan's ionic model with a Thomas-Fermi (TF) electronic component that has a correction applied to generate the correct binding energy [27]. On the other hand, 5190 included both solid and liquid phases, with the ionic component coming from Debye theory and the CRIS model [28], respectively. The electronic component included calculations using the effective medium code INFERNO [29] above 40 g/cm^3 and the Saha model [30] below 4.6 g/cm^3 with an interpolation region between. At low pressures, both tables include van der Waals loops in the liquid-vapor coexistence region. However, the 5190 table results are much better than 540L due to its use of the more accurate CRIS model. The 540X table uses the effective medium code Pergatorio [31] to compute its electronic component, and produces results qualitatively similar to 540L.

At high pressures all three tables are inaccurate in describing the experimental and DFT Hugoniot data, as seen in Fig. 2. These discrepancies appear to be due to the electronic models. The TF and effective medium models are know to be asymptotically accurate at very high compressions and temperatures, but are not accurate enough in moderate compressions. Pressure isotherms in the interpolation region of 5190 appear soft indicating that the blending of the two electronic models is responsible for the corresponding softness on the Hugoniot. Reproducing 5190 using PANDA [32], but replacing the original electronic term with Thomas-Fermi-Dirac theory [33], causes the Hugoniot to shift to nearly the same location as 540L, confirming this observation.

The new model (5191) is based upon the form of the 5190 model but with some components replaced by semi-empirical forms, including the electronic term. This allows calibration of the model to the experimental Hugoniot with good results, as seen in Fig. 2. The individual components and their parameters are described in the following subsections, along with a brief comparison with prior models.

3.1 Cold curve for xenon

The VHT cold curve form of Ref. [34] is based on the Vinet form with the limit of the Holzapfel H12 form, and TFK theory. It has been found to work well in describing the cold compression behavior for several metals. However, when the form was applied to solid xenon some deficiencies were noted in the results. In particular, while the form did meet its design criteria of mimicking the Vinet form at ambient conditions and asymptotically approaching Thomas-Fermi (TF) behavior at high compression, the intermediate region developed an unphysical loop, which could even take the cold curve to negative pressures in compression. This was a result of the method used to interpolate between the low and high compression regions. The VHT cold curve pressure has the form

$$P_c(\sigma) = a_0(Z_5 + a_1 Z_4 + a_2 Z_3) + a_3 Y^2 X \exp(a_4 X), \tag{2}$$

where $\sigma = \rho/\rho_{00}$, $Y = \sigma^{1/3}$, $X = 1 - Y^{-1}$, and $Z_n = Y^n - 1$. The constants $\{a_i\}$ depend upon the equilibrium bulk modulus K_0, its pressure derivative K_0', the equilibrium density ρ_{00}, and other fixed constants in a complex manner [34]. The cold free energy is then given by the expression

$$F_c = \int_1^\sigma P_c(x) x^{-2} dx. \tag{3}$$

The unphysical oscillation arises from the polynomial like character of the Z_n terms of Eq. (2). When the bulk modulus is sufficiently large, as for the metals studied previously, the values computed for the coefficients $\{a_i\}$ result in a smooth behavior. The bulk modulus for xenon is almost two orders of magnitude smaller than typical metals, however, and so the oscillations arise.

There are no additional adjustable parameters in the VHT cold curve and so one must add an additional term to the form to suppress the oscillations. However, solving for the zeros of Eq. (2) or its derivatives, so as to insure smooth behavior in the form, is a non-trivial exercise due to the exponential. Therefore, a new form was chosen, taking inspiration from the polynomial forms typically used in Russian EOS work [34]. The new cold curve has the form

$$P_c(Y) = \sum_{i=-1}^{5} b_i Y^i, \tag{4}$$

where the $\{b_i\}$ are constants. Unlike typical Russian forms, Eq. (4) has its maximum exponent stopping at 5, the value required by the TF limit. Thus one can naturally obtain the correct TF and Thomas-Fermi-Kirzhnits (TFK) limiting behaviors by appropriately setting the b_4 and b_5 coefficients. This leaves five unfixed coefficients. They are set by requiring that the form obeys $P_c(1) = 0$, that one recovers the desired K_0 and K_0', that the third derivative of P_c matches the Vinet form at $\sigma = 1$, and that P_c matches the Vinet pressure at $\sigma = 125/64$. Explicitly, one has the following system of seven equations,

$$\lim_{Y \to \infty} P_c(Y) = P_{TF} Y^5 \tag{5}$$

$$P_c(1) = 0 \tag{6}$$

$$K_c(1) = \frac{Y}{3} \frac{dP_c}{dY}(1) = K_0 \tag{7}$$

$$\frac{dK_c}{dP}(1) = K_0' \tag{8}$$

$$P_c(5) = P_{TFK} \tag{9}$$

$$K_c''(1) = K_V'' \tag{10}$$

$$P_c(5/4) = P_V \tag{11}$$

where $P_{TF} = 1003.59(\rho_0 Z_{av}/F)^{5/3}$ in units of GPa with Z_{av} and F respectively the average atomic number and formula weight, P_{TFK} is the TFK pressure at 125-fold volume compression, $K_V'' = 3/4 K_0(19 + 9K_0'(3K_0' - 2))$ is the value of the left hand side of Eq. (10) evaluated for the Vinet form, and $P_V = 15/16 K_0 \exp(3/10 K_0' - 1))$ is the Vinet pressure at $\sigma = 125/64$. The primes on K_c in Eq. (10) denote application of the operator $Y\frac{d}{dY}$. Clearly, Eq. (5) requires $b_5 = P_{TF}$. The remaining six equations form a linear system which may be solved using standard techniques.

Once the coefficients are known, one may explicitly calculate the roots of Eq. (4). If any real root is found for $\sigma \geq 1$, then the Vinet pressure matching constraint can be relaxed until the root is removed. A stricter criteria can also be used. In particular, for normal materials, the pressure derivative of the bulk modulus is positive and so the curvature of the cold curve is positive in compression. Thus, one can constrain the cold curve to have no roots with $\sigma \geq 1$ in its second derivative by adjusting the Vinet pressure matching constraint. In practice, for xenon this constraint was always sufficient to ensure a positive curvature, and so no adjustments were needed.

Besides the suppression of the unphysical oscillations of the VHT form, Eq. (4) also has the nice property of reduced computational complexity, since one no longer has to compute the Vinet exponential term. However, there is still a logarithmic term in the energy due to the $i = 3$ term. To speed up the computation of the polynomial form even more, one could replace the $i = 3$ term with an $i = -2$

term in Eq. (4). Although this increases the order of the polynomial of which one must find the roots, this cost is upfront so overall the reduction in effort from not having to calculate the logarithm would be substantial. Future work will investigate the appropriateness of this revision to Eq. (4).

In expansion, $\sigma < 1$, the form of Eq. (4) becomes invalid once one strays too far from equilibrium. To ameliorate this fact, a low density polynomial form is matched to Eq. (4) at a certain density ρ_{LJ}. The type of form used for F_c in this regime is dependent upon the binding characteristics of the material in question. The following Lennard-Jones based form works well in general for solids,

$$F_c(\rho) = f_1 \rho^{f_2} - f_3 \rho^{f_{LJ}} + E_B, \tag{12}$$

where E_B is the binding energy and f_{LJ} is an adjustable constant [32]. However, this form may encounter problems for some values of f_{LJ}, so the form

$$F_c(x = \rho/\rho_{LJ}) = E_B + x \sum_{i=1}^{6} f_i x^i \tag{13}$$

is also used, where f_4, f_5 are adjustable constants. In both cases, the constants f_1, f_2, and f_3 are chosen to ensure that the free energy F_c and its first two derivatives are continuous at $\rho = \rho_{LJ}$. The polynomial form of Eq. (13) may have unphysical oscillations for arbitrary choices of f_4 and f_5. Hence an additional parameter f_6 is automatically chosen such that the second derivative of Eq. (13) has no more than one zero for $0 \le x \le 1$. This prevents oscillation of the cold curve form while still allowing the physical curvature change between the equilibrium point and infinite expansion.

3.2 Thermal ionic terms

The thermal motion of the ions in the solid are modeled using Debye theory. The free energy is given as

$$F_i = \frac{R}{A}\left(\frac{9}{8}\theta + 3T \log\left(1 - \exp\left(-\frac{\theta}{T}\right)\right) - TD\left(\frac{\theta}{T}\right)\right), \tag{14}$$

where A is the molecular weight, R is the gas constant, and $D(x)$ is the Debye integral. The Debye temperature θ is given by

$$\theta = \theta_r \sigma^{\gamma_\infty} \exp((\gamma_r - \gamma)/\tau_g), \tag{15}$$

with

$$\gamma = (\gamma_r - \gamma_\infty)/\sigma^{\tau_g} + \gamma_\infty. \tag{16}$$

Here θ_r, γ_r, γ_∞, and τ_g are all constants. In expansion, the Debye model becomes unrealistic due to the inclusion of unrealistic energy states in the integral over the harmonic oscillator frequencies. Therefore, a correction is included that cuts off the integral at the frequency corresponding to the Wigner-Seitz cell radius. The result is that the free energy expression becomes

$$F_i = \frac{R}{A}\left(\frac{9}{8}\theta + F_D\left(\frac{\theta}{T}\right) - F_D\left(\frac{\theta_n}{T}\right)\right), \tag{17}$$

where

$$F_D(x) = 3T \log(1 - \exp(-x)) - TD(x) \tag{18}$$

and

$$\theta_n = 0.2 \frac{\theta^2 A M_0}{2\hbar^2} \left(\frac{3AM_0}{4\pi\rho}\right)^{2/3}. \tag{19}$$

This cuts off the unrealistic increase in pressure as the density decreases. More details are found in Ref. [32].

To model the thermal motion of the ions in the liquid state, the variational fluid model CRIS was used. This model describes a fluid using a hard sphere system as a reference and has been applied to

a variety of systems including noble gases [35] and metals [36]. Through a variational calculation of the size of fluid atoms, a good description is obtained for the compressed fluid. As well, the model exhibits van der Waal's loops and so may be used to describe the vaporization transition. Further detailed descriptions of the model may be found in Refs. [37,38]. Version 2 of the model as found in revision 2.14 of PANDA [32] was used in the calculations. There are several inputs to the model. The most important is the cold curve for the material of interest. This is input in the form described in Sec. 3.1. The other adjustable parameters are E_{fac}, herein set to zero, and B_{exp} which are used to modify the melting behavior of the model. Both the cold and thermal ion free energy terms of Eq. (1) are included in this model.

3.3 Thermal electronic terms

For the thermal electronic component, a semi-empirical electronic model developed for metals was used. The basic equations are given below, but a more detailed description may be found in Ref. [39]. The free energy is given by

$$F_e(\sigma, T) = -c_e(\sigma, T)T \log\left(1 + \frac{B_e(T)T}{2c_e(\sigma, T)}\sigma^{-\gamma_e(\sigma, T)}\right) \qquad (20)$$

where

$$B_e(T) = \frac{2}{T^2}\int_0^T\int_0^{T'}\beta(\tau)d\tau dT', \qquad (21)$$

$$\beta(T) = \beta_i + \left(\beta_0 - \beta_i + \beta_m\frac{T}{T_b}\right)\exp(-T/T_b), \qquad (22)$$

$$c_e(\sigma, T) = \frac{3R}{2}\left(Z + \frac{\sigma_z\sigma T_z^2(1-Z)}{(\sigma + \sigma_z)(T^2 + T_z^2)}\exp(-\tau_i/T)\right), \qquad (23)$$

$$\tau_i = T_i\exp(-\sigma_i/\sigma), \qquad (24)$$

and

$$\gamma_e(\sigma, T) = \gamma_i + \left(\gamma_0 - \gamma_i + \gamma_m\frac{T}{T_g}\right)\exp\left(-\frac{T}{T_g} - \frac{(\sigma - \sigma_e)^2}{\sigma\sigma_d}\right). \qquad (25)$$

Here Z is the atomic number, R is the gas constant, and $\sigma = \rho/\rho_r$. The remaining parameters are all adjustable, although they have connections to physical effects. In particular, these equations describe the asymptotic limits of the electron gas as well as ionization and the metal-insulator transition.

At very high temperatures the electronic component may require adjustment due to the parameter calibration performed on lower temperature data. To accomplish this, an interpolation to TFK theory was included in the model. The interpolation uses quintic polynomials to ensure second derivative continuity in the thermodynamic functions. Details are found in Ref. [40]. The low temperature bound for interpolation was 16 eV at densities greater than 1 g/cm^3 and was gradually reduced for smaller densities to a minimum of approximately 2.5 eV.

3.4 Results and comparisons

The new EOS contains both solid and fluid phases. The solid uses the series VHT cold curve with LJ expansion form, the Debye model, and the thermal electronic model. The fluid uses the CRIS model with a separate series VHT cold curve with the expansion form of Eq. (13). It also uses a simplified version of the thermal electronic model where the second term in the exponential of Eq. (25) is eliminated, the heat capacity is set to a constant $c_e = 3RZ/2$, and $\gamma_m = 0$. An energy shift E_s is included to obtain the correct enthalpy change at melt. The final parameters of both models are listed in Table 1. They were calibrated to a range of experimental and calculated data. This data included

Table 1. Parameters and their values for model 5191.

| Solid model parameters			
ρ_{00}	3.8232 g/cm^3	T_i	40000. K
K_0	3.7866 GPa	T_g	300000. K
K'_0	7.2903	σ_z	0.9
ρ_{LJ}	3.7808 g/cm^3	σ_e	1.0
f_{LJ}	2.5394	σ_d	2.5
E_B	0.12588 MJ/kg	σ_i	0.3
θ_r	48.890 K	β_i	2.0299e-10 MJ/kg/K^2
ρ_r	3.5033 g/cm^3	β_0	1.8789e-10 MJ/kg/K^2
γ_r	2.6285	β_m	4.0004e-11 MJ/kg/K^2
γ_∞	0.66667	γ_i	0.23503
γ_τ	1.0	γ_0	0.40218
T_b	5026.4 K	γ_m	1.4
T_z	200000. K		
Fluid model parameters			
ρ_{00}	3.7604 g/cm^3	E_s	0.00446 MJ/kg
K_0	3.6487 GPa	ρ_r	7.2159 g/cm^3
K'_0	7.5131	T_b	12827. K
ρ_{LJ}	3.7228 g/cm^3	T_g	38318. K
f_4	-0.49799 MJ/kg	β_i	7.8369e-09 MJ/kg/K^2
f_5	0.010932 MJ/kg	β_0	1.0006e-12 MJ/kg/K^2
f_6	0.049799 MJ/kg	β_m	3.4958e-08 MJ/kg/K^2
E_B	0.12301 MJ/kg	γ_i	0.23434
B_{exp}	2.0901 g$^{1/3}$/cm	γ_0	0.21
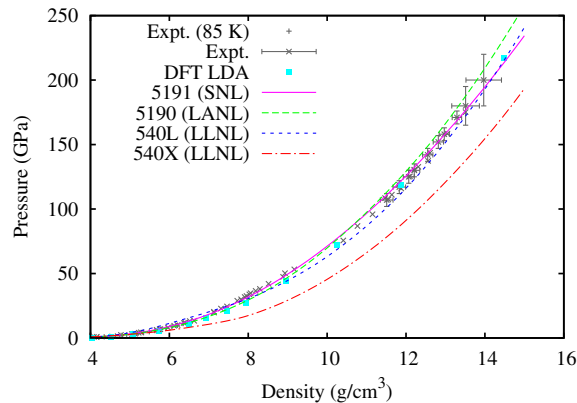
Fig. 3. Xenon compression at 298 K. Experimental DAC data [41] at 85 K is shown as gray pluses. DAC data at 298 K is shown as gray exes [42–45]. DFT calculations for the liquid are shown as cyan squares. Results for the tables 5191, 5190, 540L and 540X are shown as solid magenta, dashed green, short dashed blue, and dot-dashed red lines respectively.

parametrizations of the experimental measurements and DFT calculations of the Hugoniot, isothermal compression, and melting curve, as well as experimental measurements of the critical region.

As already seen in Fig. 2 the new model 5191 improves on prior EOS models, agreeing very well with experimental and theoretical Hugoniot date through the entire range of available pressures. A sample of the isothermal compression data was also included, which highlights the relative importance of the cold and thermal terms in the EOS. A more detailed picture of the 298 K isotherm is shown in Fig. 3. Here all the available experimental data is shown along with DFT calculations. While there are some small difference between them, the 540L, 5190, and 5191 models all are in agreement with
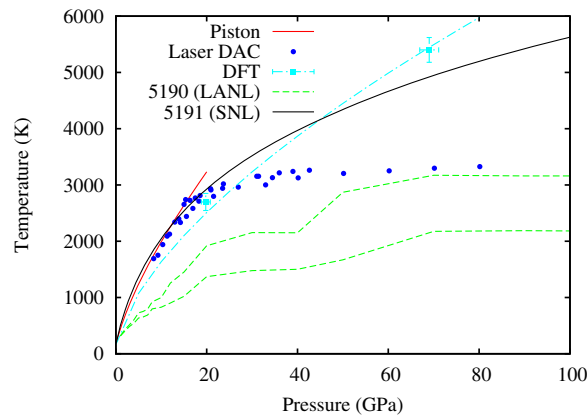
Fig. 4. Xenon melt curves. The red line shows experimental data from blocked capillary [46] and piston [47] experiments extrapolated up from 0.8 GPa using a Simon melt curve. Blue circles show laser heated DAC measurements [1,48]. DFT calculations [49] are given by the cyan squares and dot-dash line. The dashed green lines denote the melting bounds for the 5190 table and the magenta line the melt curve for the 5191 model.
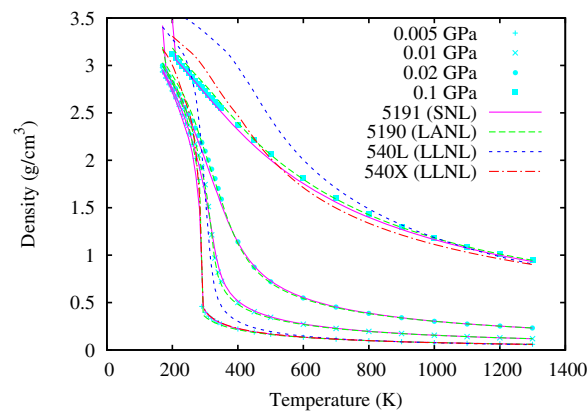

Fig. 5. Xenon isobars in the region of the critical point. Experimental data [53,54] is shown at 0.005 GPa, 0.01 GPa, 0.02 GPa, and 0.1 GPa using cyan pluses, exes, circles, and squares respectively. Lines are as in Fig. 3. For clarity, only the 0.005 GPa and 0.1 GPa lines are shown for 540L and 540X.

the isothermal compression data. The 540X model is notably soft, already falling well outside of the experimental data above two-fold volume compressions.

The melting of xenon under pressure has been the subject of intense scrutiny and discussion over the last decade, as shown in Fig. 4. High-pressure DAC results show a plateau while low-pressure piston experiments and DAC experiments in the lower pressure range agree with a traditional melting process. First-principles simulations yield a high-melting point [50] while diamond anvil experiments up to 80 GPa [51] show a flat melting curve. A similar discrepancy between DAC and DFT data was very recently resolved in the case of Ta [52]. In that work, Dewaele et al. show how sensitive the results are to changes in experimental conditions [52]. The current work parametrized a normal melt curve beyond 20 GPa, as shown in Fig. 4. Of the prior models, only 5190 contains melt. However, it does not describe the experimental or theoretical data well except at zero pressure.

Finally, Fig. 5 shows density isobars in the critical region of the phase diagram. The new table 5191 and 5190 both agree very well with experimental data in this important region. On the other hand, 540L and 540X shown notable differences to the data. There are two factors at play here. First 5190 and 5191 both use the CRIS model which was initially developed to model the liquid-vapor coexistence of the noble gases [35]. So the agreement points to the success of that model. Secondly, the disagreements

found in 540L and 540X are in part due to the lack of a true multi-phase EOS and in particular the inclusion of the melting transition. As seen in Fig. 3, 540L agrees well with the solid data. At high temperatures it agrees well with the liquid data in Fig. 5. In between it interpolates between the two behaviors, but since it does not include the melt transition, and thus the volume change on melting, it cannot agree with the liquid data near the melt temperature. The situation for 540X is similar. However, it appears to sacrifice agreement with the solid data to provide better agreement at low temperatures with the liquid data. Even so, there are significant deviations below 300 K in the liquid density.

4 Summary and discussion

We have performed shock compression measurements on liquid xenon up to pressures of 840 GPa. The experimental results validated the Hugoniot points calculated using the DFT methods. The results of the new experimental and DFT work, together with existing literature data at lower pressure, provided a basis for the development of a new xenon EOS model. The new model was tabulated on a fine density-temperature grid to aid in preserving phase boundary information and is available from the public Los Alamos SESAME database as table number 5191. Note that the 5191 table contains Maxwell constructions in all regions of phase coexistence. The new model 5191 shows improvement over all prior models in the description of the xenon Hugoniot. Additionally, it provides a similarly good agreement as 5190 to data in the region of the liquid-vapor critical point. Lastly, the multiphase model contains a significantly improved melt curve in comparison to 5190.

References

1. R. Boehler, M. Ross, P. Söderlind, D.B. Boercker, Phys. Rev. Lett. **86**, 5731 (2001)
2. W. Nellis, M. v. Thiel, A. Mitchell, Phys. Rev. Lett. **48**, 816 (1982)
3. T.R. Mattsson, R.J. Magyar, in *Shock Compression of Condensed Matter – 2009*, edited by M. L. Elert *et al.* (AIP, Melville, New York, 2009), Vol. 1195 of *AIP Conf. Proc.*, pp. 797–800
4. M. D. Knudson *et al.*, Phys. Rev. Lett. **87**(22), 225501 (2001)
5. M.P. Desjarlais, Phys. Rev. B **68**(6), 064204 (2003)
6. M. D. Knudson *et al.*, Science **322**(5909), 1822 (2008)
7. M. French, T.R. Mattsson, N. Nettelmann, R. Redmer, Phys. Rev. B **79**, 054107 (2009)
8. T.R. Mattsson, J.M.D. Lane, K.R. Cochrane, M.P. Desjarlais, A.P. Thompson, F. Pierce, G.S. Grest, Phys. Rev. B **81**, 054103 (2010)
9. S. Root *et al.*, Phys. Rev. Lett. **105**, 085501 (2010)
10. R. W. Lemke *et al.*, J. Appl. Phys. **98**, 073530 (2005)
11. L.M. Barker, R.E. Hollenbach, J. Appl. Phys. **43**, 4669 (1972)
12. D. L. Hanson *et al.*, in *Shock Compression of Condensed Matter – 2001*, edited by M. D. Furnish *et al.* (AIP, Melville, New York, 2001), Vol. 620 of *AIP Conf. Proc.*, p. 1141
13. S. M. Thornberg, private communication
14. A.J. Leadbetter, H.E. Thomas, Trans. Faraday Soc. **61**, 10 (1965)
15. G.E. Duvall, R.A. Graham, Rev. Mod. Phys. **49**, 523 (1977)
16. M.D. Knudson, M.P. Desjarlais, Phy. Rev. Lett. **103**, 225501 (2009)

17. G. Kresse and J. Hafner, Phys. Rev. B **47**, R558 (1993), Phys. Rev. B **49**, 14251 (1994); G. Kresse and J. Furthmüller, Phys. Rev. B **54**, 11169 (1996).
18. P. E. Blöchl, Phys. Rev. B **50**, 17953 (1994); G. Kresse and D. Joubert, Phys. Rev. B **59**, 1758 (1999).
19. A.E. Mattsson, P.A. Schultz, M.P. Desjarlais, T.R. Mattsson, K. Leung, Modelling Simul. Mater. Sci. Eng. **13**, R1 (2005)
20. N. Mermin, Phys. Rev. **137**, A1441 (1965)
21. R. Armiento, A.E. Mattsson, Phys. Rev. B **72**, 085108 (2005)
22. A. E. Mattsson *et al.* , J. Chem. Phys. **128**, 084714 (2008)
23. P. Haas *et al.*, Phys. Rev. B **79**, 085104 (2009)
24. H.B. Radousky, M. Ross, Phys. Lett. A **129**, 43 (1988)
25. V. D. Urlin *et al.*, High Press. Res. **8**, 595 (1992)
26. K. A. Goettel *et al.*, Phys. Rev. Lett. **62**, 665 (1989)
27. LEOS 540 is based on QEOS, R. M. More et al. Phys. Fluids 31, 3059 (1988).
28. G.I. Kerley and P.M. Henry, SESAME 5190, in Los Alamos National Laboratory Report No. LA-8062, (January, 1980).
29. D.A. Liberman, Phys. Rev. B **20**, 4981 (1979)
30. S.G. Brush, Prog. High Temp. Phys. Chem. **1**, 1 (1967)
31. P. A. Sterne *et al.*, High Energy Density Physics **3**, 278 (2007)
32. G.I. Kerley, Tech. Rep. SAND88-2291, Sandia National Laboratories (1991)
33. R.D. Cowan, J. Ashkin, Phys. Rev. **105**, 144 (1957)
34. J.H. Carpenter, I.V. Lomonosov (2007), unpublished
35. G.I. Kerley, Tech. Rep. LA-4760, Los Alamos Scientific Laboratory (1971)
36. G.I. Kerley, Int. J. Impact Engng. **5**, 441 (1987)
37. G.I. Kerley, J. Comp. Phys. **73**, 469 (1980)
38. G.I. Kerley, J. Comp. Phys. **73**, 478 (1980)
39. A. V. Bushman *et al.*, *Intense dynamic loading of condensed matter* (Taylor & Francis, Washington DC, 1993)
40. J.H. Carpenter, Tech. Rep. SAND2007-6907, Sandia National Laboratories (2007)
41. K. Syassen, W.B. Holzapfel, Phys. Rev. B **18**, 5826 (1978)
42. A.P. Jephcoat, H.K. Mao, L.W. Finger, D.E. Cox, R.J. Hemley, C.S. Zha, Phys. Rev. Lett. **59**, 2670 (1987)
43. A.N. Zisman, I.V. Aleksandrov, S. Stishov, Phys. Rev. B **32**, 484 (1985)
44. K.A. Goettel, J.H. Eggert, I.F. Silvera, W.C. Moss, Phys. Rev. Lett. **62**, 665 (1989)
45. R. Reichlin, K.E. Brister, A.K. McMahan, M. Ross, S.M. tin, Y.K. Vohra, A.L. Ruoff, Phys. Rev. Lett. **62**, 669 (1989)
46. A. Michels, C. Prins, Physica **28**, 101 (1962)
47. P.H. Lahr, W.G. Eversold, J. Chem. Engng. Data **7**, 42 (1962)
48. M. Ross, R. Boehler, P. Söderlind, Phys. Rev. Lett. **95**, 257801 (2005)
49. A.B. Belonoshko, S. Davis, A. Rosengren, R. Ahuja, B.J. ansson, S. I. Simak, L. Burakovsky, D.L. Preston, Phys. Rev. B **74**, 054114 (2006)
50. A.B. Belonoshko, S. Davis, A. Rosengren, R. Ahuja, B. Johansson, S.I. Simak, L. Burakovsky, D.L. Preston, Phys. Rev. B **74**, 054114 (2006)
51. M. Ross, R. Boehler, P. Soderlind, Phys. Rev. Lett. **95**, 257801 (2005)
52. A. Dewaele *et al.*, Phys. Rev. Lett. **104**, 255701 (2010)
53. W.B. Streett, L.S. Sagan, L.A.K. Staveley, J. Chem. Thermodynamics **5**, 633 (1973)
54. N.B. Vargaftik, *Tables on the Thermophysical Properties of Liquids and Gases in Normal and Dissociated States* (Hemisphere Publishing Corporation, Washington, D.C., 1975), p. 580